TU Delft

Delft University of Technology

Electrical modeling of cylindrical dielectric elastomer transducers

van Kessel, R.; Bauer, P.; Ferreira, J. A.

DOI
10.1088/1361-665X/abde4f

Publication date
2021

Document Version
Final published version

Published in
Smart Materials and Structures

Citation (APA)
van Kessel, R., Bauer, P., & Ferreira, J. A. (2021). Electrical modeling of cylindrical dielectric elastomer transducers. *Smart Materials and Structures*, *30*(3), Article 035021. https://doi.org/10.1088/1361-665X/abde4f

Important note
To cite this publication, please use the final published version (if applicable).
Please check the document version above.

Copyright
Other than for strictly personal use, it is not permitted to download, forward or distribute the text or part of it, without the consent of the author(s) and/or copyright holder(s), unless the work is under an open content license such as Creative Commons.

Takedown policy
Please contact us and provide details if you believe this document breaches copyrights.
We will remove access to the work immediately and investigate your claim.

This work is downloaded from Delft University of Technology.
For technical reasons the number of authors shown on this cover page is limited to a maximum of 10.

Smart Materials and Structures

PAPER • **OPEN ACCESS**

Electrical modeling of cylindrical dielectric elastomer transducers

To cite this article: R van Kessel *et al* 2021 *Smart Mater. Struct.* **30** 035021

View the article online for updates and enhancements.

This content was downloaded from IP address 145.94.96.203 on 01/03/2021 at 08:22

OPEN ACCESS
IOP Publishing
Smart Materials and Structures
Smart Mater. Struct. **30** (2021) 035021 (14pp)
https://doi.org/10.1088/1361-665X/abde4f

Electrical modeling of cylindrical dielectric elastomer transducers

R van Kessel[1,2], **P Bauer**[2] **and J A Ferreira**[3]

[1] SBM Offshore, 24 Avenue de Fontvieille—P.O. Box 199, MC 98007 Monaco Cedex, Monaco
[2] DC Systems, Energy Conversion & Storage group, Faculty of Electrical Engineering, Mathematics and Computer Science, Delft University of Technology, Delft, The Netherlands
[3] Power Electronic & EMC group, Faculty of Electrical Engineering, Mathematics and Computer Science, University of Twente, Enschede, The Netherlands

E-mail: c.l.vankessel@tudelft.nl

Received 11 November 2020, revised 23 December 2020
Accepted for publication 21 January 2021
Published 10 February 2021

Abstract

Dielectric elastomer transducers (DETs) are commonly modeled by lumped-element models (LEMs), however such models do not capture the cutoff behavior that manifests at relatively low frequencies due to the high resistivity of the stretchable electrodes. Moreover, the contribution of the electrodes into the lumped series resistance is not accurately known. The aim of this work is to define the accuracy and frequency limits of the LEM and to derive the exact values of its lumped components. This is achieved by developing a detailed three-dimensional distributed-element model (DEM) of the transducer structure. Based thereon, analytical expressions are developed for the LEM components and limits are explored. Through numerical evaluation of the DEM it is found that only two-third of the single-polarity electrode resistance contributes to the lumped series resistance, which is three times lower than predicted by existing models. Comparison between the LEM and DEM further shows that the LEM is adequate for frequencies significantly below the cutoff frequency. Thereafter, capacitance and resistance fall off as a result of signal propagation limitations. This has been experimentally verified. The developed DEM and established validity range of the simple LEM allows for more accurate sensors and better optimized transducers designs, with up to three times less electrode material.

Keywords: electroactive polymer, dielectric elastomer, transducer, generator, distributed element model, lumped element model, energy harvesting

(Some figures may appear in colour only in the online journal)

1. Introduction

Dielectric elastomer transducers (DETs) are soft, electrostatic transducers that can operate as sensors, actuators and generators. Their monolithic structure promises silent, maintenance-free and with specific materials even bio-compatible devices, which can be manufactured by modern techniques such as printing and spraying.

Since the early publications of [1, 2], these favorable characteristics have triggered the development of a wide variety of applications such as artificial muscles and soft robotics [3–5], medical devices [6, 7], pneumatic pumps [8] and valves [9]. Generator applications include human energy scavengers [10], rotational harvesters [11] and wave energy conversion [12]; and wearable sensors [13] for sensing in e.g. smart healthcare.

An example of a large-scale generator application is the S3 Wave Energy Converter (WEC) [14]. A concatenation of cylindrical DETs forms an elastic tube of several hundred

Original Content from this work may be used under the terms of the Creative Commons Attribution 4.0 licence. Any further distribution of this work must maintain attribution to the author(s) and the title of the work, journal citation and DOI.

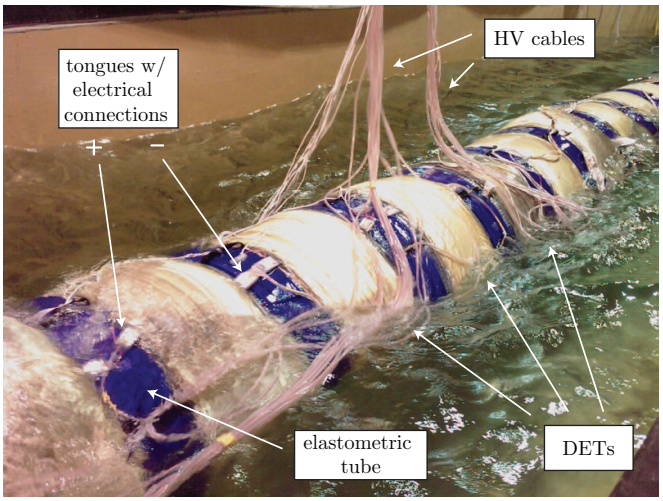

Figure 1. DETs deployed on early WEC prototype.

meters of length. Radial deformations are induced by a tuned resonance with the wave pressure field. The resulting variation in capacitance is converted directly into electrical energy by power electronics [15–17]. Figure 1 shows DETs on an elastomeric tube as part of an early prototype.

DETs consist of dielectric elastomer (DE) film layers sandwiched between compliant electrodes of opposite polarity. The transducer forms a deformable capacitor, the capacitance of which varies with strain. By applying voltage, an electric field is established in the active region where the electrodes overlap. The resulting Maxwell stress exerts a mechanical pressure on the elastomer film, reducing its thickness and expanding its lateral area. In the opposite generator mode, a mechanical source acts against the Maxwell stress, increasing the separation of opposite charges. The subsequent increase in electrostatic potential energy is harvested by an electrical circuit.

The stretchable electrode is a key design element of the transducer. Whereas the dielectric determines the energy density [18], the electrode is decisive for the power density. The requirement of being stretchable and ability to sustain repeated cycling limits the material choice however. Typical materials are thin metallic electrodes, corrugated to accommodate strain, and carbon-based composites [19]. The latter are more common and have better fatigue characteristics, yet the conductivity is much lower, with sheet resistances orders of magnitude above the $10\,\Omega/\mathrm{sq}$ of MPP capacitors [20]. The composite electrodes are also much thicker, thereby reducing the energy density and introducing considerable stiffness that limits the actuation strain. There is thus a strong drive to minimize the electrode thickness in the design, leading to higher resistance.

Accurate electrical models are key to the design and efficient operation of DETs. Lumped-Element Models (LEMs) are widely used, with variable capacitance C, dielectric loss resistance R_p and electrode resistance R_s [21, 22]. Multilayer transducers are then modeled by a parallel connection of LEMs [23].

However, the existing LEMs for DETs have two important shortcomings. First, they do not account for signal propagation limitations introduced by the high resistance of the stretchable electrode and large transducer geometry. Already at low frequency (e.g. 100 Hz) signals may no longer penetrate the entire structure. Second, the contribution of the electrode resistance to account for in the LEM is not exactly known. It is often determined experimentally [23], or it is simply assumed that both electrodes contribute in full to the series losses [22], which proves over-conservative.

More detailed models based on transmission lines have been developed for modeling the field distribution [24]. Most DETs have electrical contacts on opposite ends however, which excludes the use of two-port networks and thus transmission line theory.

Distributed-element models (DEMs) are able to cope with diffusion problems and different contact configurations, and are commonly used for high frequency film capacitors [20, 25].

The aim of this paper is to develop a DEM for cylindrical DETs for the purpose of defining how much of the electrode resistance should be accounted for in the LEM and for quantifying the cutoff frequency that results from the highly resistive electrodes. Linkage between the DEM and LEM is demonstrated and the frequency limits of the LEM are defined.

This is the first of a set of papers dealing with the electrical modeling and design of cylindrical DETs. Subsequent papers build upon the developed electrical model and cover the design aspects for optimal operation in a given application.

The remainder is organized as follows. Section 2 presents the transducer arrangement and key design parameters, based on which a DEM is developed in section 3. The impedance calculation method is disclosed in section 4. After translating the DEM into a simplified LEM model in section 5, both models are evaluated numerically in section 6 for determining the series resistance factor and cutoff behavior. Experimental validation of the model is presented in section 7, the conclusions in section 8.

2. Arrangement of cylindrical transducers

Cylindrical DETs are constructed around a capacitive film stack, comparable to wound axial capacitors. Having a much larger geometry and stretchable structure, the arrangement typically consists of (a) a capacitive DE film stack, (b) an inner and outer grounded conductive shield layer for electrical safety, (c) an inner and outer encapsulation for mechanical protection, (d) circumferential liquid metal channels on each side to reduce series resistance [26], (e) extrusions on each side creating a strain-free zone for the transition from stretchable to solid conductor. Figure 2 illustrates this arrangement.

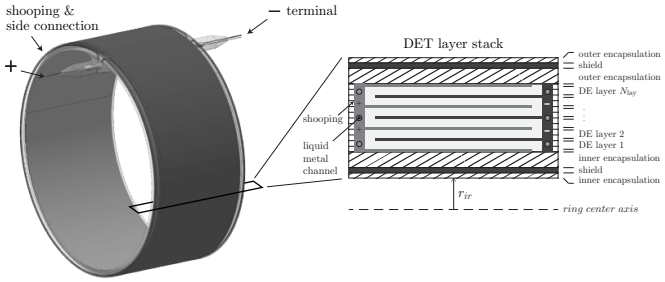

Figure 2. Typical arrangement of cylindrical DET.

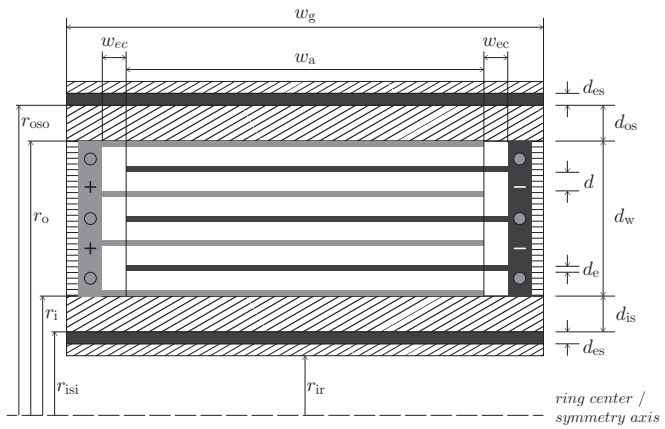

Figure 3. Parametrization of cylindrical transducer film stack.

Focus of this work is on the differential impedance between the positive and negative terminal. Presence of shields, or any other conductive medium surrounding the transducer, is therefore neglected.

2.1. Capacitive film stack

The film stack is composed of dielectric elastomer layers alternated with stretchable electrodes of alternating polarity. Electrodes of same polarity are terminated at the designated ring side, with sufficient edge clearance at the opposite end to avoid breakdowns. The area in which electrodes of both polarities overlap is the active film width w_a and determines the total capacitor area, along with the winding length.

In the context of the winding, the number of layers N_{lay} refers to the number of individual dielectric layers. The thickness of each turn then comprises the DE film thickness d plus the thickness of a single electrode d_e, ergo $d_t = d + d_e$. The total winding thickness then becomes $d_w = r_o - r_i = N_{lay}\, d_t + d_e$.

The exact composition and parametrization of the film stack is depicted in figure 3. Typical design parameters along with representative values for a WEC application are listed in table 1.

2.2. Construction

The film stack is typically constructed by a continuous winding process, in which two lengths of pre-manufactured

Table 1. Typical values of key design parameters.

Measure	Symbol	Value	Unit
Winding inner radius	r_i	510	mm
Winding outer radius	r_o	550	mm
Active width	w_a	750	mm
Edge clearance	w_{ec}	20	mm
Electrode thickness	d_e	30	μm
Dielectric thickness	d	100	μm
Channel radius	r_{ch}	0.5	mm

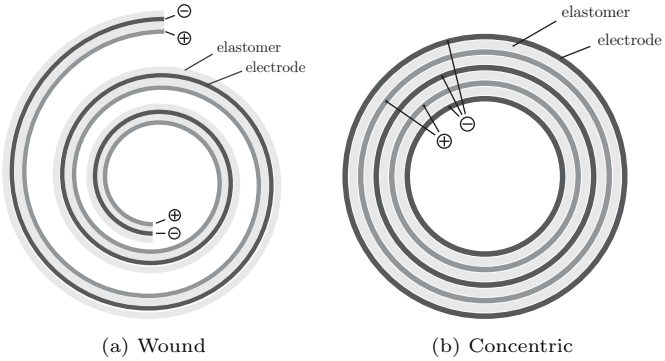

Figure 4. Typical construction methods (side view).

elastomer film with single-sided electrode are co-wound on a removable mandrel. The result is a wound stack of continuous length, as shown in figure 4(a). Another method comprises a layer-by-layer deposition process, such as obtained by spraying or printing. This method results in a concentric film stack as shown in figure 4(b).

Focus of this work is on wound constructions, although it can be demonstrated that both constructions are equivalent for large radius to thickness ratios.

2.3. Contact configuration

Two common configurations for the electrical contacts are shown in figure 5. With single-ended contacts (SEC), the two polarities connect at the same location of the capacitive structure. Such configuration may be applied in single-layer planar transducers, or wound transducers without shooping side connection. With double-ended contacts (DEC), the two polarities connect at opposite ends of the structure. This is a common configuration for multilayer capacitive structures and typically yields low impedance structures as each layer has a direct connection through shooping.

3. Electrical model development

This section deals with the development of a DEM for the capacitive film stack of the DET. Other components such as cables may be included externally as separate lumped elements.

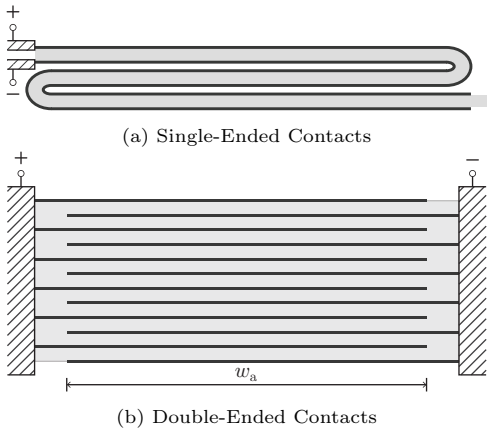

Figure 5. Typical contact configurations.

3.1. Key assumptions

The main assumption is that the circumferential resistance is much lower than the cross-contact resistance of the electrode stack, such that the current gradient is primarily oriented axially. Given the aim of this work, the transducer is further analyzed being static, with zero strain. In addition:

(i) Non-dispersive medium: permittivity and permeability are independent of the frequency of the applied field.
(ii) Non-dispersive medium: permittivity is independent of the frequency of the applied field.
(iii) Linear medium: the electrical properties do not depend on the magnitude of the applied field.
(iv) Isotropic material: the properties of the elastomer and its electrodes are uniform in all directions.
(v) Large area to thickness ratio: fringing fields at the electrode edges negligible.
(vi) Mechanically static: the rate of change in the mechanical domain is much smaller than in the electrical domain, ergo time derivatives of C'_d, R'_d, R'_e are not taken into account.
(vii) Resistive components are assumed dominant over inductive components in the frequency range of interest, the latter are therefore neglected.
(viii) Modeling contact resistance is strongly dependent on construction and materials of transducer, particularly shooping and side connection, and therefore disregarded: $R'_{co} = 0$.
(ix) Equal electrode resistivity for both polarities—as opposed to e.g. electrolytic capacitors.

3.2. Modeling approach

The DET three-dimensional (3D) physical structure is decomposed into axial slices. These slices are subsequently divided into a multiplicity of small capacitive sections. The model complexity reduction process is shown in figure 6 and consists of the following steps that are indicated in the figure accordingly:

(i) Division of circumference into N_{slice} axial slices, interconnected through liquid metal channel resistance R'_{peri}. Assuming:
  (a) resistance in circumferential direction much lower than in axial direction, i.e. $R'_{peri} \ll R'_e$. Satisfied by liquid metal channel and/or selected slice geometry. Consequently, circumferential current gradient is neglected and the axial slice is treated as isolated, multilayered one-dimensional (1D) network.
  (b) symmetry plane—for every angle θ an opposite angle exists with equal circumferential current flow. Only one half plane of the DET is thus to be modeled, with half the slices $N_{slice}/2$, each at half the impedance $Z'_{axial}/2$.
(ii) Extraction of axial slices consisting of a stack of concentric electrodes of alternating polarity.
(iii) Simplification of concentric axial slices into a Multilayer Sheet Structure (MLSS) of flat sheets by assuming the diameter to be much larger than winding height.
(iv) Transformation of MLSS into a two-dimensional (2D) DEM
(v) Reduction of multilayer model into equivalent single-layer network by folding capacitive sections around the electrode axes and accumulating the component values.

The model is developed and populated as follows. First, the properties of a single layer in the axial slice are derived in section 3.3.3. Based thereon, the full MLSS is defined in section 3.3.4, which is subsequently reduced to an equivalent single layer network (ESLN) in section 3.3.5. Finally, the model is completed in section 3.4 by cascading angular sections consisting of the ESLN and the circumferential resistance elements.

3.3. Distributed element model of multilayer sheet structure

The MLSS shown in steps 3–4 of figure 6 contains the capacitive sections from the length and thickness direction of the axial slices and is modeled using a DEM. The parameter values of the infinitesimal elements in the model depend on material properties, transducer geometry and model order.

3.3.1. Winding length. The total winding length is a resultant of the transducer geometry and increases progressively with radius. The winding is considered a spiral starting at $\varphi_i = 2\pi r_i/d_t$ and terminating at $\varphi_o = 2\pi r_o/d_t$, both angles being cumulative and referenced to the spiral center. The exact winding length for this configuration equals:

$$l_w = \frac{d_t}{4\pi}\left[\varphi_o\sqrt{\varphi_o^2+1} + \sinh^{-1}(\varphi_o) - \varphi_i\sqrt{\varphi_i^2+1} - \sinh^{-1}(\varphi_i)\right]. \quad (1)$$

For definition of the capacitive sections and in line with the assumption of relatively large diameter ($r_i \gg d_w$), the mean length of turn (MLT) l_{mlt} and mean radius of turn (MRT) r_{mrt} are defined as:

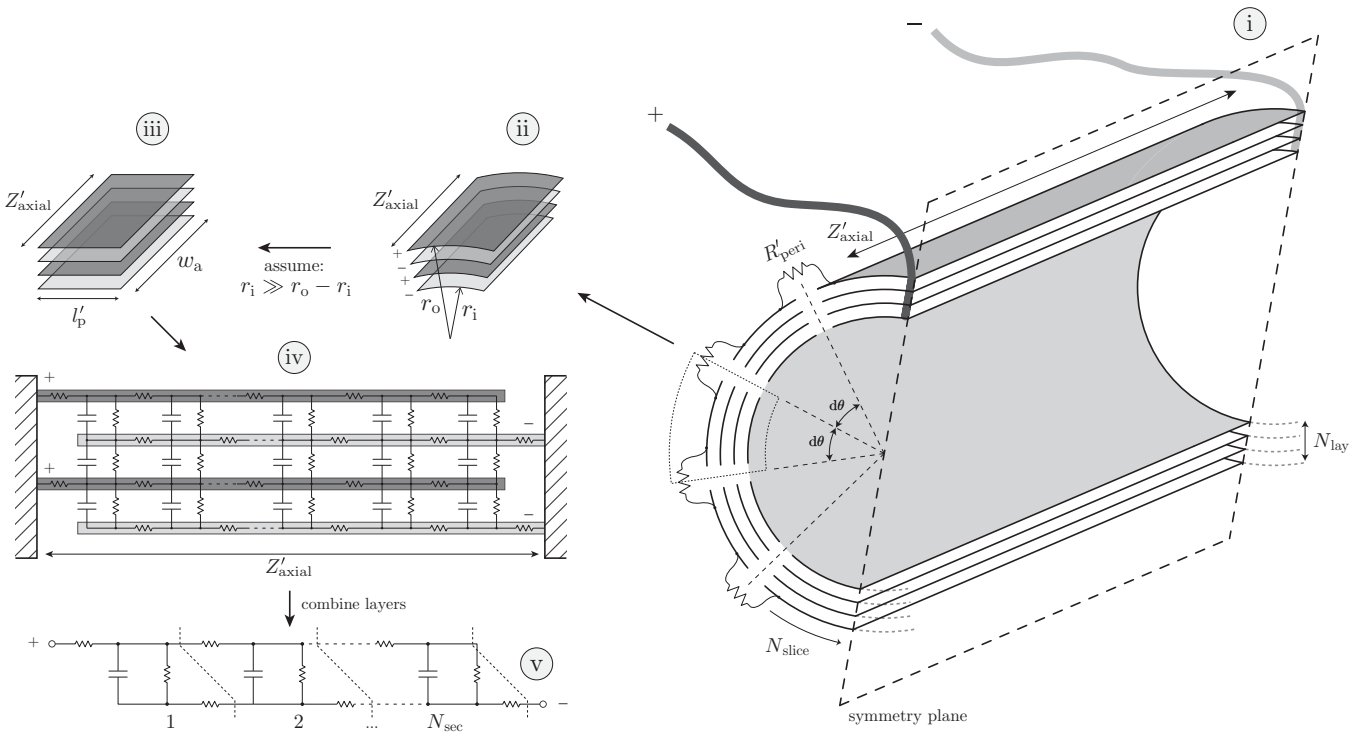

Figure 6. Decomposition of cylindrical DET into equivalent set of axial slices.

$$l_{mlt} = \frac{l_w}{N_{lay}} \tag{2}$$

$$r_{mrt} = \frac{l_w}{2\pi N_{lay}}. \tag{3}$$

3.3.2. Number of sections. The number of sections determines the resolution and accuracy of the model. Along its circumference, the DET is divided into N_{slice} axial slices. Each of the resulting MLSS is subdivided into N_{sec} sections. When taking into account the symmetry plane, the model order is thus $\frac{1}{2}N_{slice}N_{sec}$.

3.3.3. Single-layer properties. The elementary sections in the MLSS are calculated by analyzing a single film layer from said multilayer structure as illustrated in figure 7. The single layer is divided into N_{sec} capacitive cells, each with length w'_a and width l'_p as follows:

$$l'_p = \frac{l_{mlt}}{N_{slice}} = \frac{l_w}{N_{slice}N_{lay}} \tag{4}$$

$$w'_a = \frac{w_a}{N_{sec}}, \tag{5}$$

where the $'$-notation indicates sectional quantities.

With cell geometry defined, the electrical elements can be calculated accordingly. The cell capacitance C'_d, dielectric leakage resistance R'_d and electrode resistance R'_e are given by:

$$C'_d = \epsilon_0\epsilon_r\frac{l'_p w'_a}{d} \tag{6}$$

$$R'_d = \rho_d\frac{d}{l'_p w'_a} \tag{7}$$

$$R'_e = \frac{\rho_e}{d_e}\frac{w'_a}{l'_p}. \tag{8}$$

Here, ϵ_0 denotes the permittivity of free space, ϵ_r the relative permittivity or simply dielectric constant and ρ_d the dielectric elastomer resistivity. The electrode material resistivity and thickness are denoted by ρ_e and d_e respectively, the ratio of which commonly referred to as sheet resistance $R_{e,sheet} = \rho_e/d_e$.

In addition to the capacitive cells, the single layer further contains resistive elements to account for the electrode clearance region and contact resistance. The edge clearance resistance is given by:

$$R'_{ec} = \frac{\rho_e}{d_e}\frac{w_{ec}}{l'_p}. \tag{9}$$

The contact resistance represents all components and interfaces from the liquid metal channel up to the electrode edge. As stated in section 3.1, it is strongly dependent on implementation and therefore not considered in this work: $R'_{co} = 0$.

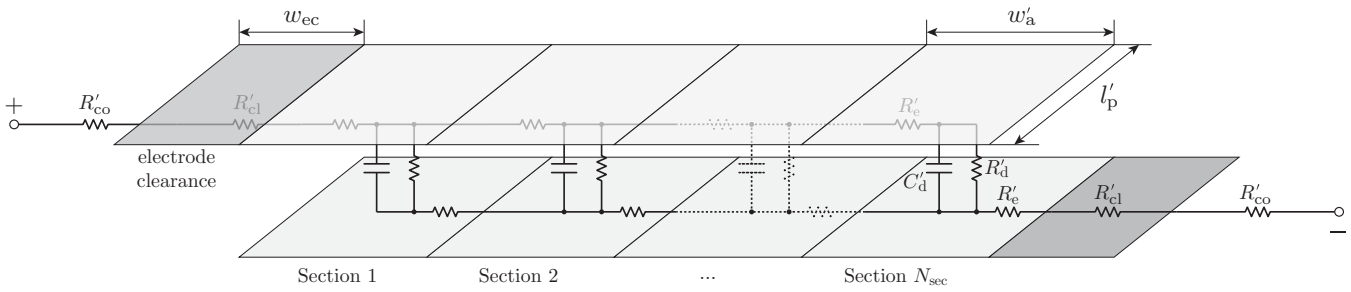

Figure 7. Parametrization of single film layer in axial slice.

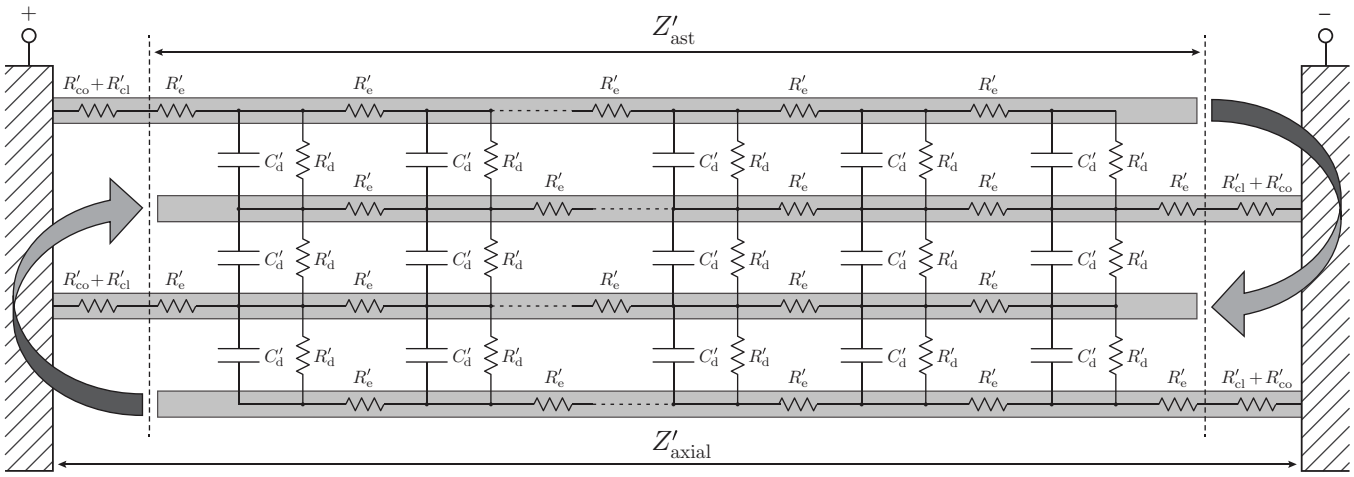

Figure 8. Distributed-element model of an axial slice.

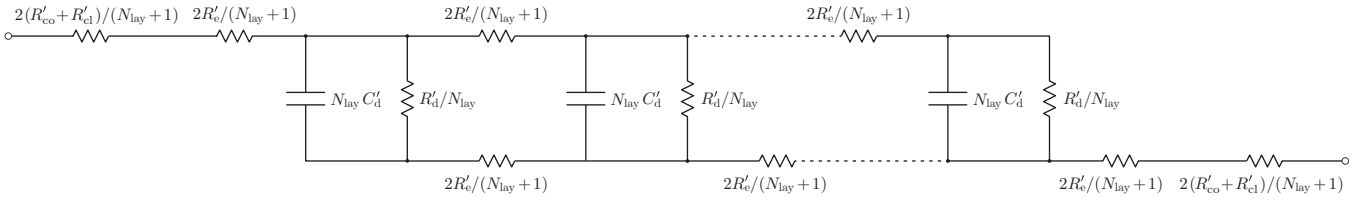

Figure 9. Equivalent single layer network of multilayer sheet structure.

3.3.4. Multilayer sheet structure. Under the assumption of large diameter to thickness ratio (figure 6), all layers in the transducer winding are considered to be located on the MRT and therefore have equal length. As a result, all layers in the MLSS have identical properties, and the electrical elements defined for the single layer network in the former section can be used.

The MLSS consists of electrode clearance and contact resistances terminating each layer, and of an active stack in which the electrodes of both polarities overlap. The latter is referred to as active stack and is modeled by Z'_{ast}. Figure 8 shows the fully developed MLSS.

3.3.5. Equivalent single layer network. The MLSS can be reduced to an ESLN given the identical layer properties and by using the folding technique demonstrated in [20]. This is illustrated by the arrows in figure 8. Layers are folded around the respective electrode axes until only a single layer remains. Stacked sections are connected in parallel and the impedance of the receiving section is proportionally reduced by the number of sections accumulated. An odd number of layers is required to satisfy assumption item (i).

The derived ESLN is depicted in figure 9. In this equivalent network, the electrical elements equal:

$$C'_{d,esln} = C'_d N_{lay} \tag{10}$$

$$R'_{d,esln} = R'_d / N_{lay} \tag{11}$$

$$R'_{e,esln} = 2R'_e/(N_{lay}+1). \tag{12}$$

Noteworthy is the factor two in the electrode resistance, which signifies the electrode being shared by the upper and

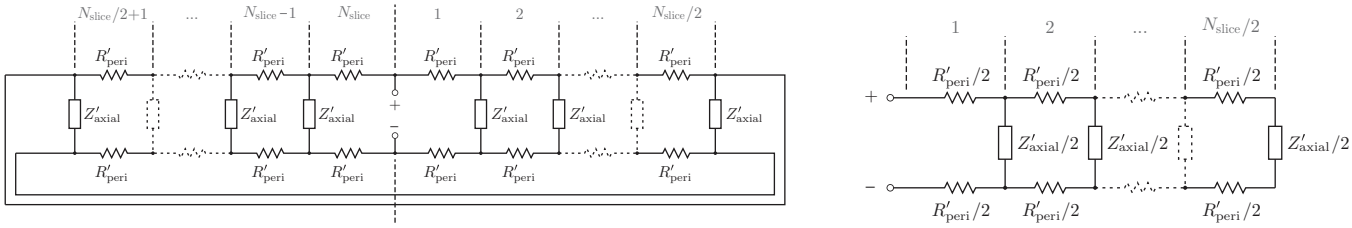

(a) interconnection of axial slices into ring-shaped DEM model

(b) single-ended equivalent of ring-shaped DEM

Figure 10. Full DET model by interconnection of axial slices into ring-shaped DEM.

lower dielectric layer. The result is double the current density compared to the single-layer case, and, thus, double the electrode resistance. Contact and edge resistance are not given explicitly but scale equally with the electrode.

3.4. Full transducer model by cascading slices

Last in the development of the full 3D DET model is the connection of the axial slices into a ring structure as per figure 10(a). The interconnection is through sectional resistance R'_{peri}, which is defined as:

$$R'_{peri} = R_{peri}/N_{slice}, \tag{13}$$

where R_{peri} is the resistance of all liquid metal channels and shooping materials over the full circumference of one side of the DET.

The symmetry in figure 10(a) is easily identified and rearranging yields the single-sided network of figure 10(b), in which both Z'_{axial} and R'_{peri} appear at half the value.

4. Calculating the transducer impedance

The full 3D transducer model thus constitutes a single-ended network that contains the double-ended axial slices represented by the ESLN of figure 9 and interconnected through the sectional circumferential resistances. The impedance of the axial slice is computed first, then the full model impedance is calculated as cascade.

4.1. Axial slice impedance

The impedance of the MLSS is computed analytically using nodal analysis from classical linear electric circuit theory. The double-ended configuration rules out commonly used models based on cascaded two-port models, such as transmission lines, as the port condition is not fulfilled.

Labeling each node of the DEM in figure 9 and developing the nodal equations yields the admittance matrix of the structure. Solving the set of equations for the node voltages then allows computation of the terminal current. The impedance is finally calculated as ratio of terminal voltage and current.

Generation of the admittance matrix for an arbitrary number of sections N_{sec} is automated in a MATLAB model. Using the Symbolic Math Toolbox, the system of nodal equations is solved and the impedance is computed symbolically. Results

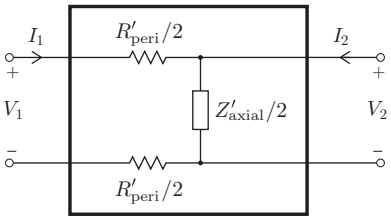

Figure 11. Two-port definitions for angular section.

from the model have been cross-validated with the SimScape Electrical Impedance Measurement blockset.

As example, the impedance of the active stack represented by a DEM with $N_{sec} = 4$ sections equals:

$$Z'_{ast|_{N_{sec}=4}} = \frac{R'_d}{N_{lay}}\left[\frac{1}{4+4j\omega C'_d R'_d} + \frac{7N_{lay}R'_e}{R'_d(N_{lay}+1)} + \frac{R'_e}{4R'_e + 2R'_d(1/N_{lay} + 2j\omega C'_d R'_e + 1)}\right]. \tag{14}$$

The impedance of the axial slice finally equals:

$$Z'_{axial} = 4\frac{R'_{co} + R'_{ec}}{N_{lay}+1} + Z'_{ast}. \tag{15}$$

4.2. Full transducer model

The full model comprises a cascade of axial slices as per figure 10(b). The sections in this model are in single-ended configuration and meet the port condition. The full model can therefore be analyzed using two-port methods. The transmission parameter representation is selected for the ease of cascading using simple matrix multiplication.

Sections in the full model are referred to as angular sections and comprise the axial slice and perimetrical resistance. Figure 11 shows the applied port definitions for such section, which is governed by the following relation:

$$\begin{bmatrix} V_1 \\ I_1 \end{bmatrix} = \begin{bmatrix} t_{11} & t_{12} \\ t_{21} & t_{22} \end{bmatrix} \begin{bmatrix} V_2 \\ -I_2 \end{bmatrix} = \boldsymbol{T} \begin{bmatrix} V_2 \\ -I_2 \end{bmatrix}, \tag{16}$$

here, $\boldsymbol{T}$ denotes the transmission matrix with elements t_{ii} the t-parameters. It can be shown that the transmission matrix for the angular section equals:

$$\boldsymbol{T}_{as} = \begin{bmatrix} 1 + 2R'_{peri}/Z'_{axial} & R'_{peri} \\ 2/Z'_{axial} & 1 \end{bmatrix}. \tag{17}$$

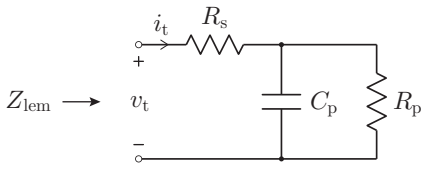

Figure 12. Lumped-element model of DET.

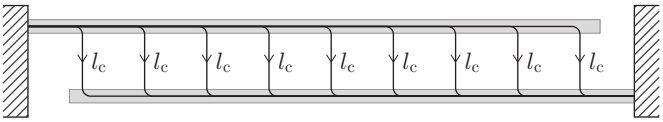

Figure 13. Uniform current path length in MLSS.

Now the cascade of angular sections becomes a simple matrix multiplication, such that the transmission matrix of the full DET model simply becomes:

$$\boldsymbol{T}_{\text{det}} = [\boldsymbol{T}_{\text{as}}]^{N_{\text{slice}}/2}, \tag{18}$$

where the exponent $N_{\text{slice}}/2$ reflects the symmetry.

The impedance of the DET is finally obtained by evaluating the input impedance of the network described by $\boldsymbol{T}_{\text{det}}$. Ergo:

$$Z_{\text{det}} := Z_{\text{in}} = \frac{V_1}{I_1}\bigg|_{I_2=0} = \frac{t_{\text{det},11}}{t_{\text{det},21}}, \tag{19}$$

with $t_{\text{det},11}$ and $t_{\text{det},21}$ elements of $\boldsymbol{T}_{\text{det}}$.

5. Simplified electrical model

The DEM defined in the former sections is rather unpractical for simply modeling the first-order behavior of DETs. One of the aims of this work is therefore to map the results of the detailed DEM to the commonly used LEM.

5.1. Lumped-element model

The simplified model comprises the LEM of figure 12, for which the impedance is given by:

$$Z_{\text{lem}} = R_s + \frac{R_p}{1 + j\omega C_p R_p}. \tag{20}$$

Capacitance C_p and parallel resistance R_p account for the dielectric material and are easily calculated using the total area of the active film winding:

$$C_p = \epsilon_0 \epsilon_r \frac{l_w w_a}{d} = C'_d (N_{\text{slice}} N_{\text{sec}} N_{\text{lay}}) \tag{21}$$

$$R_p = \rho_d \frac{d}{l_w w_a} = R'_d / (N_{\text{slice}} N_{\text{sec}} N_{\text{lay}}). \tag{22}$$

Series element R_s is more complex to determine as *a priori* it is not known how the electrodes of the active stack manifest in the lumped series resistance. By identifying in figure 13 that the current path length in the slice equals the film width ($l_c \approx w_g$) independent of location, element R_s is expressed as function of the transducer width as follows:

$$R_s = \frac{\rho_e}{d_e}\frac{1}{l_w}\frac{2N_{\text{lay}}}{N_{\text{lay}}+1}\left[\alpha_{\text{rs}} w_a + 2w_{\text{ec}}\right] + \alpha_{\text{rs}}\frac{R_{\text{peri}}}{4}, \tag{23}$$

where $2N_{\text{lay}}/(N_{\text{lay}}+1)$ accounts for the multilayer structure as found for the ESLN series elements.

The first term in equation (23) relates to the effective series resistance of the active stack. It is calculated as the resistance of all electrode layers of one polarity in parallel, over the active width as $R_{\text{elect}} = \rho_e w_a/(d_e l_w)$. Further, α_{rs} is a scaling factor that expresses how much of this electrode resistance contributes to the lumped series resistance. It is determined by numerical analysis in section 6.3.1.

The second term in equation (23) relates to the electrode side terminations. The contact and clearance resistances appear as separate items in series with the active stack (see e.g. figure 9), and are therefore included separately and without scaling factor.

The third term in equation (23) relates to the side resistance. One may identify that the single-sided ring network of figure 10(b) constitutes a DEM similar to the MLSS, but with SEC and only a single layer. Factor α_{rs} is found to be equal for SEC and DEC and thus equally factors in the effective contribution of the circumferential resistance in the lumped R_s. Factor $1/4$ finally accounts for the ring symmetry, with axial slices of half the impedance cascaded over half the length.

5.2. Generalization using time constants

For generalization of the model and defining design guidelines, the main results are presented relative to the time constants of the lumped-element circuit. The basis is thus a linear, first order circuit that does not exhibit any diffusion limitations. As such, these constants constitute theoretical quantities and especially the series variant is hard to obtain empirically by the higher-order behavior of the structure (cut-off).

5.2.1. Series time constant. For voltage-driven circuits or high frequencies, the dynamics resp. losses are dominated by the series resistance. By considering $R_p \gg R_s$, the series time constant equals:

$$\tau_s = R_s C_p, \tag{24}$$

As figure of merit, the series time constant may be expressed as function of only the active stack resistance, which is often dominant in large transducers with liquid metal channel (esp. $w_a \gg w_{\text{ec}}$ and $N_{\text{lay}} \gg 1$). Working out equation (24) then yields the time constant as function of design and material parameters only:

$$\tau_s \approx 2\alpha_{\text{rs}}\epsilon_0\epsilon_r \frac{\rho_e}{d_e}\frac{w_a^2}{d}, \tag{25}$$

which most notably varies squared with active width.

5.2.2. Parallel time constant. For current-driven circuits or low frequencies, the dynamics resp. losses are dominated by the parallel (dielectric) resistance. By neglecting the series resistance, the parallel time constant becomes:

$$\tau_\mathrm{p} = R_\mathrm{p} C_\mathrm{p} = R'_\mathrm{d} C'_\mathrm{d}, \tag{26}$$

which is independent of geometry and a property of the dielectric material only.

5.2.3. Relative operating frequency. Most phenomena captured by the DEM are a function of the excitation frequency f_exc in relation to the structure's time constants. For generalization, the results are therefore analyzed using relative frequency $f_\mathrm{exc}\,\tau$, which simply represents the ratio between the time constant and signal period: τ / T_exc.

5.2.4. Loss tangents. The time constants and the relative frequency derived therefrom are closely related to the commonly used loss tangents. For the series loss dominant case, loss factor $\tan\delta_\mathrm{s}$ equals:

$$\tan\delta_\mathrm{s} = \omega C_\mathrm{p} R_\mathrm{s} = 2\pi \left(\frac{\tau_\mathrm{s}}{T_\mathrm{exc}} \right) = 2\pi f_\mathrm{exc} \tau_\mathrm{s}. \tag{27}$$

And for the loss factor $\tan\delta_\mathrm{p}$ of the parallel loss dominant case:

$$\tan\delta_\mathrm{p} = \frac{1}{\omega C_\mathrm{p} R_\mathrm{p}} = \frac{1}{2\pi} \left(\frac{T_\mathrm{exc}}{\tau_\mathrm{p}} \right) = (2\pi f_\mathrm{exc} \tau_\mathrm{p})^{-1}. \tag{28}$$

6. Numerical model analysis

The developed DEM is evaluated numerically for validation of the defined LEM component values and for quantifying the frequency range in which the LEM accurately governs the electrical behavior of the DET.

6.1. Approach

The different parts of the full model are analyzed separately and under specific conditions. First, the active stack of the MLSS structure is evaluated for analyzing the effective series resistance and cut-off behavior due to the finite electrode resistance. Second, the full model is evaluated for assessing the effect of the finite circumferential resistance. For the latter, concrete parameter values are used for illustration.

For evaluation purposes, the transducer impedance is decomposed into equivalent series resistance (ESR) and -capacitance (ESC) components of the Rs-Cs network model as follows:

$$r_\mathrm{s} = \Re\{Z_\mathrm{det}\} \tag{29}$$

$$c_\mathrm{s} = -\left(2\pi f \Im\{Z_\mathrm{det}\}\right)^{-1}. \tag{30}$$

Table 2. Electrical parameters for numerical evaluation.

Parameter	Symbol	Value	Unit
Relative permittivity	ϵ_r	2.7	—
Dielectric resistivity	ρ_d	1×10^{14}	Ωm
Liquid metal resistivity	ρ_g	3×10^{-7}	Ωm
Electrode sheet res.	$R_\mathrm{e,sheet}$	2.0	kΩ/sq
Number of layers	N_lay	307	—
Number of slices	N_slice	500	—
Number of sections	N_sec	500	—
Element length	w'_a	1.50	mm
Element width	l'_p	6.68	mm
Element capacitance	C'_d	2.39	pF
Element resistance	R'_d	999	TΩ
Element electrode res.	R'_e	674	Ω
Element clearance res.	R'_ec	8.99	kΩ
Perimetrical resistance	R_peri	1.23	Ω
Sectional perimetrical res.	R'_peri	2.5	mΩ

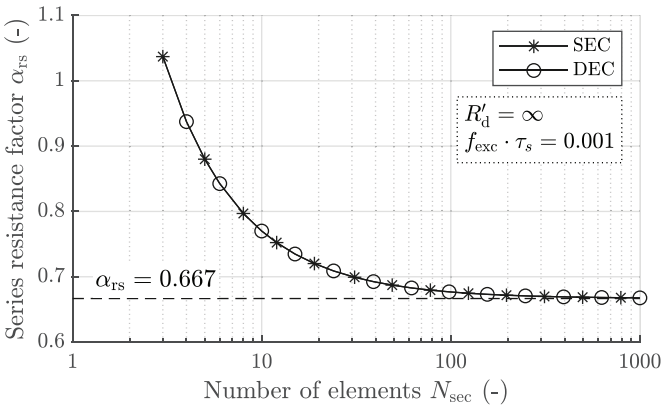

Figure 14. Convergence of series resistance factor.

6.2. Evaluation parameters

The model is analyzed with the design parameters listed in table 1. A single liquid metal channel is assumed on each side. The model parameters are summarized in table 2. Model order is selected for convergence, see e.g. figure 14.

6.3. Active stack analysis

For generalization, the active stack is studied as separate part, thus with clearance and circumferential resistance set to zero. Parallel resistance R'_d is omitted to study effect of finite electrode resistance only. It would have to be unrealistically low to shunt C'_d and have any tangible impact on the diffusion.

6.3.1. Lumped series resistance factor. Factor α_rs is determined by evaluating the ESR of the active stack in relation to the lumped expression. The number of elements in the model is varied to find convergence. The evaluation frequency is selected below cut-off at $0.001/\tau_\mathrm{s}$, which corresponds to 1.7 Hz for the present parameters.

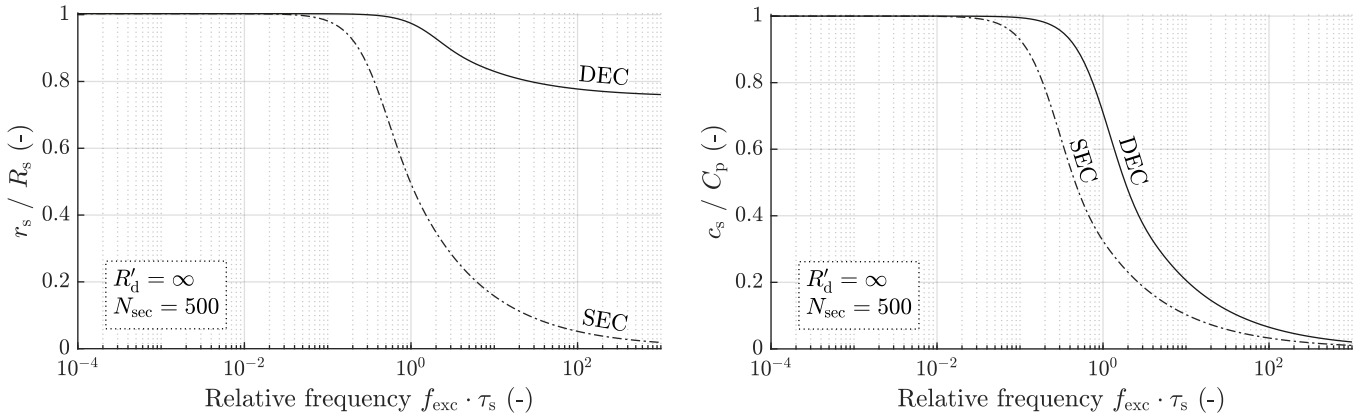

(a) Equivalent Series Resistance (b) Equivalent Series Capacitance

Figure 15. Equivalent series network values of active stack calculated with DEM relative to lumped model values.

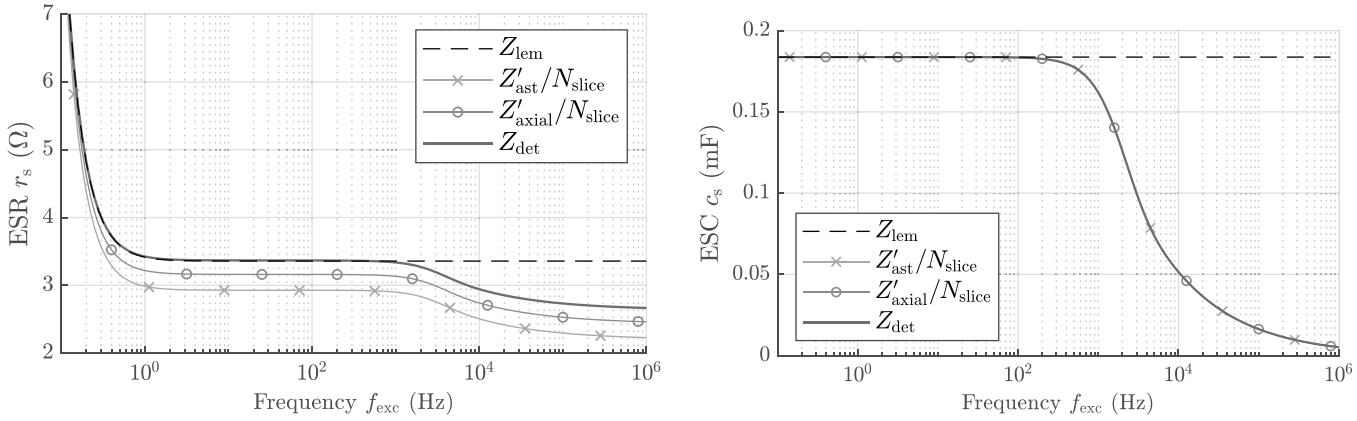

(a) Equivalent Series Resistance (b) Equivalent Series Capacitance

Figure 16. Calculated equivalent series network values for full DET model. Dashed lines represent LEM values.

Figure 14 shows that the factor is independent of contact configuration and equals:

$$\alpha_{rs} = \lim_{N_{sec}\to\infty} \frac{r_s}{R_{elect}} \approx 2/3, \tag{31}$$

where R_{elect} denotes the resistance of all electrode layers of one polarity in parallel as noted in section 5.1.

The series resistance factor thus reveals that only $2/3$ of the *single* polarity electrode length (l_c) manifests in the lumped R_s. Runs with different cell aspect ratios and electrode resistivities have confirmed the generalized results.

6.3.2. Cut-off operation. When the signal propagation time of a structure exceeds the period of the applied signal, the energy flow is reduced and the system is in cutoff. In cutoff region, diffusion effects are non-negligible and the observed resistance and capacitance fall off sharply with frequency. Such cutoff behavior is captured by the DEM, but not by the simple LEM, which affects its validity.

For expressing the validity limits of the LEM, the cutoff frequency of the lumped circuit is taken as basis. The cutoff frequency of such first-order linear circuit equals:

$$f_c = \frac{1}{2\pi\tau_s}. \tag{32}$$

Validity of the LEM is defined here as the frequency range in which the lumped capacitance C_p is within 0.1% of the ESC of the DEM. The upper limit frequency f_{lim} is then defined as:

$$c_s(f_{lim}) = 0.999 \times C_p. \tag{33}$$

Figures 15(a) and (b) present the ESR and ESC calculated with the DEM. These are normalized to frequency independent lumped model values R_s and C_p. By inspection:

(a) Validity limit (-0.1%) for SEC: $f_{lim} = 0.01/\tau_s$
(b) Validity limit (-0.1%) for DEC: $f_{lim} = 0.05/\tau_s$

Hence, the limit frequency of the LEM equals $0.071 \times f_c$ for SEC and $0.28 \times f_c$ for DEC. Beyond the limit frequency, both series resistance and capacitance fall off progressively, and the LEM is no longer valid. For DEC, the resistance

Table 3. Sample properties in experimental validation.

Parameter	Sym.	Value	Uncert.	Unit
Sample width	w_s	58	± 1	mm
Sample length	l_s	145	± 1	mm
Thickness dielectric	d_s	402	± 10	μm
Relative permittivity	ϵ_r	2.7	± 0.1	—
Dielectric resistivity	ρ_d	3×10^{13}	—	Ωm

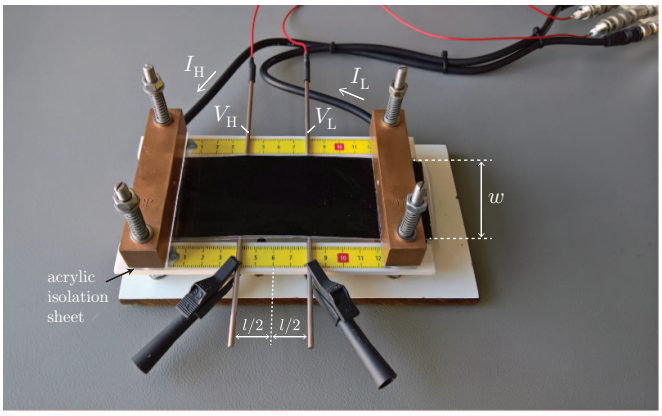

Figure 17. Sheet resistance 4 W measurement setup.

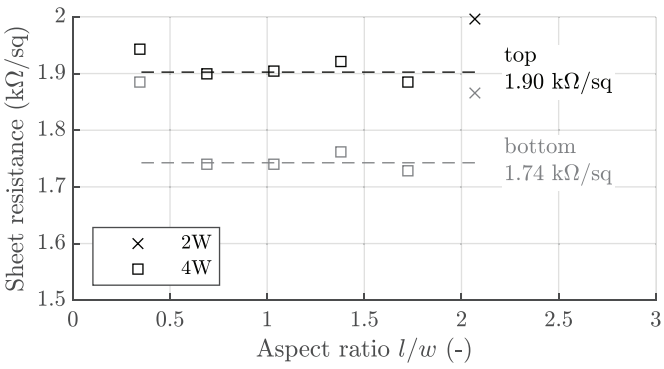

Figure 18. Measured electrode sheet resistance.

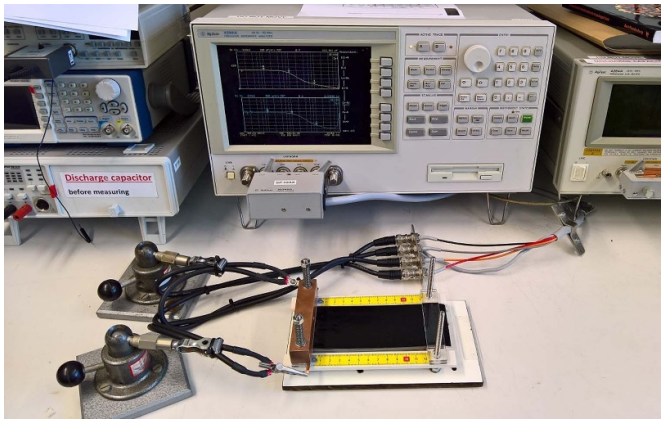

Figure 19. Impedance measurement setup.

falls off less sharply with frequency, despite a progressively lower capacitance. This is explained by current still propagating from one end to another end of the structure, as opposed to the SEC case where the signal simply no longer penetrates the entire structure.

Figure 15(b) is particularly useful for transducer design. For a given operating frequency f_{exc}, it provides the maximum allowable time constant for the active stack to avoid cutoff behavior. As example, for a transducer with DEC that is to operate at 100 Hz, the series time constant shall not exceed 0.5 ms for utilizing 99.9% of the capacitance.

It is recalled that edge clearance and circumferential resistances have been omitted. For assessing the x-axis of the graphs in figure 15 one should thus use the series time constant of the active stack alone, or rely on the former factors being negligible, which is often the case.

6.4. Full DET model analysis

The calculated ESR and ESC of full model impedance Z_{det} are reported in figure 16, along with those of the LEM simplified model impedance Z_{lem}.

For comparison, the graphs also include the impedance of the active stack Z'_{ast} and axial slice Z'_{axial}. These sectional quantities are divided by the number of slices to represent full transducer scale.

The main observation is that up to the cut-off frequency, the LEM model accurately describes the impedance of the full model with active stack, clearance and circumferential resistance. Mismatch between the LEM and DEM is less than 0.3% at $0.1 \times f_c$. This suggests that the developed analytical expression for lumped resistance R_s of equation (24) takes into account the different parts correctly.

It is further observed that the ESR of the active stack is dominant. Additional resistance introduced by the edge clearance and circumferential resistance is low given the large active-to-clearance width ($w_a \gg w_{ec}$) and highly conductive liquid metal channel, respectively.

For the ESC, one may observe that the cutoff behavior in the full model is equal to the active stack. This is because the additional clearance resistances in the axial slices are external components not affecting the internal diffusion. Second, cut-off of the ring network with axial slices is at much higher frequencies due to the liquid metal channel.

7. Experimental validation of active stack

As core of the transducer model, the active stack model has been validated experimentally. A single-layer structure has been used, i.e. $N_{lay} = 1$. The sample consists of a lamination of two PDMS films, each with a composite PDMS-carbon electrode on one side. Zero edge clearance was present and the sample has never been elongated. Table 3 lists the sample properties. Stated uncertainties relate to 95% confidence level and include both instrument and estimated human error.

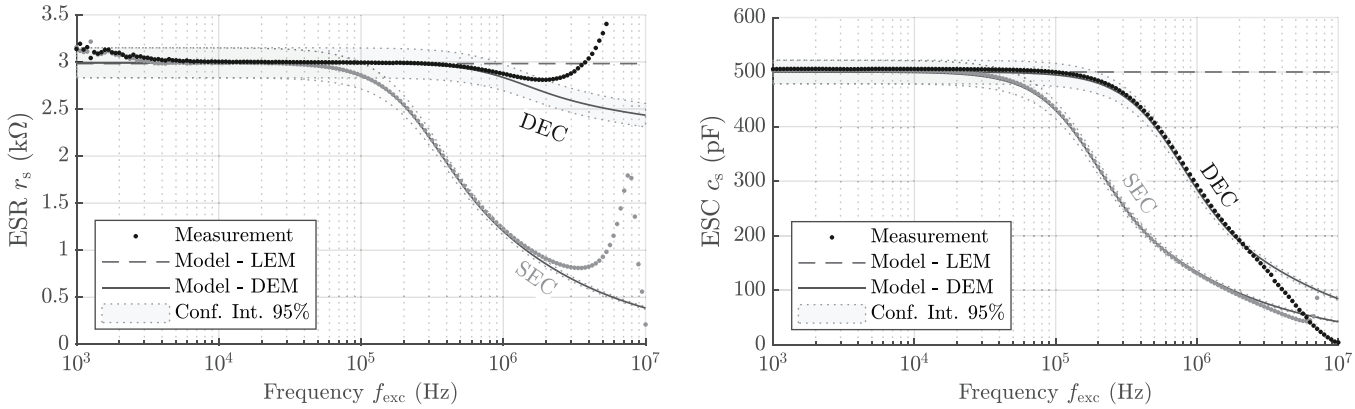

(a) Equivalent Series Resistance

(b) Equivalent Series Capacitance

Figure 20. Experimental results of single-sheet sample.

7.1. Determination of electrode sheet resistance

The sheet resistance of the composite electrodes has been determined using an Agilent 34 401A 6.5 digit Digital Multi Meter (DMM). A 4-wire (4W) configuration was used to minimize contact resistance impact. The sample has been installed in the custom measurement cell of figure 17. The bottom side of the sample rested on polished copper bars connected to the DMM's current output. Two acrylic spacers were added on the top side for electrical isolation. Constant contact pressure was exerted by means of springs forcing down another set of copper bars.

The 4W circuit was completed by moveable copper rods as voltage probes. Distance between the rods was varied and thus the aspect ratio of the electrode l/w. At each point, resistance was measured after a relaxation period of 1 min.

Figure 18 reports the calculated sheet resistance. The mean sheet resistance of top and bottom electrode is 1.90 and 1.74 $\mathrm{k\Omega/sq}$, respectively. The data points of the error-prone small aspect ratio of $l/w = 0.34$ and the 2-wire (2W) measurement have been omitted. The minor dispersion in the results may be attributed to measurement error and electrode material inhomogeneity.

7.2. Impedance and cutoff behavior

The electrical impedance of the sample has been measured over frequency to validate the modeled cutoff behavior. Both single- and double-ended contact configurations were tested.

Electrical contacts were made at the sample extremities by means of 3 mm wide copper strips running over the full width of the sample. At the contact locations, these copper strips bridge the electrode resistance. The experimental data has been corrected to compensate for the low-ESR capacitance created by the copper contact strips.

The sample was mounted between two acrylic spacers that formed the substrate for the copper strips. The acrylic spacers were in turn surrounded by the copper bars, and installed in the custom measurement cell. Limited contact pressure was applied to minimize deformation of the flexible dielectric elastomer.

The impedance was measured using an Agilent 4294A Precision Impedance Analyzer. A 4 W configuration was used up to the crocodile clips connecting to the copper strips, see figure 19. Open-Short compensation was applied with the clips as OSL reference plane. Measurement accuracy has been validated by reference measurements on similarly sized capacitors and a PCB of similar dimensions.

Figure 20 presents the measured impedance by the ESR and ESC. The graph also contains the calculated impedance of the active stack using the LEM and DEM models. The LEM has been populated in accordance with (21)–(23), the DEM with (10)–(12). Confidence intervals (95%) have been derived to account for uncertainty in the model inputs, such as sample geometry and electrical properties, under the assumption of normal distributions for the respective variables and uncorrelated error sources.

The close agreement between measured and calculated values in figure 20 confirm that the cutoff behavior is well described by the DEM and that the analytical expressions for the lumped model values are accurate. E.g. the observed ESR of $r_s = 3.00\ \mathrm{k\Omega}$ approaches two-third of the single-polarity electrode resistance of $R_{e,sheet} \times (l_s/w_s) = 4.55\ \mathrm{k\Omega}$ as average of top and bottom electrode, as predicted by equation (31).

Discrepancies in the ESR and to a lesser extent the ESC at higher frequencies may be attributed to stray inductance and the non-ideal electrical contact placements.

8. Conclusion

This work has developed a 3D-equivalent distributed-element model for cylindrical DETs to analyze the transducer impedance and effects of the high electrode resistance. It was found that the limited propagation speed of signals in the structure leads to a loss of capacitance and resistance at relative low frequencies. This cutoff behavior is not captured by the widely used LEM.

By means of the DEM it has been shown that the simple LEM represents the electrical behavior accurately (within

0.1%) for frequencies up to 0.071 and 0.28 times the lumped cutoff frequency for single- resp. double-ended contacts. At higher frequencies, the cutoff behavior results in a loss of series resistance and capacitance, which is not captured by the LEM. In practice, as demonstrated in a future publication, the transducer operating frequency is at least two orders of magnitude below the cutoff frequency for efficiency reasons. For most applications, the LEM is thus adequate. Only for transducer applications that operate closer to the lumped cutoff frequency, one may need to consider the DEM.

Analytical expressions for the series resistance in the lumped model were derived, including electrode, edge clearance and circumferential resistance contributions. By numerical evaluation of the DEM it was found that only two-third of the single-polarity electrode resistance contributes to the lumped series resistance, which is three times less than predicted by existing models. As a result, better design optimization can be performed, resulting in transducers with less electrode material and thus higher energy density and actuation strain.

The developed DEM and expressions for the LEM were verified experimentally.

Future work is to extend the model to non-static conditions by incorporating mechanical strain, which is expected to drastically impact the cutoff frequency by the combined effect of reduced thickness and increased resistivity of the carbon-based electrode. For accurately representing thick cylindrical DET such as artificial muscles, the assumption of large radius-to-thickness ratio is further to be removed. Finally, neglecting the circumferential current gradient by assuming a highly conductive side connection is to be verified experimentally. This requires a transducer with precisely defined geometry and consistent manufacturing and material properties. Such transducer also allows for further validation of multilayer structures, supplementing the single-layer experiments of this work.

Acknowledgments

The authors would like to thank Bart Roodenburg for his support and helpful advices on the experimental setup. This work was supported by SBM Offshore in the framework of the S3 Wave Energy Converter development.

ORCID iDs

R van Kessel https://orcid.org/0000-0002-2022-8630
P Bauer https://orcid.org/0000-0003-4328-7171

References

[1] Pelrine R E, Kornbluh R D and Joseph J P 1998 Electrostriction of polymer dielectrics with compliant electrodes as a means of actuation *Sensors Actuators* A **64** 77–85
[2] Pelrine R, Kornbluh R, Pei Q and Joseph J 2000 High-speed electrically actuated elastomers with strain greater than 100 *Science* **287** 836–9
[3] Gu G-Y, Zhu J, Zhu Li-M and Zhu X 2017 A survey on dielectric elastomer actuators for soft robots *Bioinspir. Biomimet.* **12** 011003
[4] Liu L, Zhang C, Luo M, Chen Xi, Li D and Chen H 2017 A biologically inspired artificial muscle based on fiber-reinforced and electropneumatic dielectric elastomers *Smart Mater. Struct.* **26** 085018
[5] Pfeil S, Henke M, Katzer K, Zimmermann M and Gerlach G 2020 A worm-like biomimetic crawling robot based on cylindrical dielectric elastomer actuators *Frontiers Robot. AI* **7** 9
[6] Chavanne J A J-M 2019 Cylindrical Dielectric Elastomer Actuator for Cardiac Assist Device (Lausanne: EPFL) (https://doi.org/10.5075/epfl-thesis-9397)
[7] Calabrese L, Frediani G, Gei M, De Rossi D and Carpi F 2018 Active compression bandage made of electroactive elastomers *IEEE/ASME Trans. Mechatronics* **23** 2328–37
[8] Linnebach P, Rizzello G and Seelecke S 2020 Design and validation of a dielectric elastomer membrane actuator driven pneumatic pump *Smart Mater. Struct.* **29** 075021
[9] Giousouf M and Kovacs G 2013 Dielectric elastomer actuators used for pneumatic valve technology *Smart Mater. Struct.* **22** 104010
[10] Jean-Mistral C, Beaune M, Vu-Cong T and Sylvestre A 2014 Energy scavenging strain absorber: application to kinetic dielectric elastomer generator *Proc. SPIE* **9056** 90561H
[11] Zhang J W, Lai Z H, Rao X X and Zhang C L 2020 Harvest rotational energy from a novel dielectric elastomer generator with crank-connecting rod mechanisms *Smart Mater. Struct.* **29** 065005
[12] Moretti G, Papini G P R, Righi M, Forehand D, Ingram D, Vertechy R and Fontana M 2018 Resonant wave energy harvester based on dielectric elastomer generator *Smart Mater. Struct.* **27** 035015
[13] Zhang H, Wang M Y, Jisen Li and Zhu J 2016 A soft compressive sensor using dielectric elastomers *Smart Mater. Struct.* **25** 035045
[14] Jean P, Wattez A, Ardoise G, Melis C, Van Kessel R, Fourmon A, Barrabino E, Heemskerk J and Queau J P 2012 Standing wave tube electro active polymer wave energy converter **8340** 83400C
[15] van Kessel R, Czech B, Bauer P and Ferreira J A 2010 Optimizing the dielectric elastomer energy harvesting cycles pp 1281–6 (https://doi.org/10.1109/IECON.2010.5675554)
[16] van Kessel R, Wattez A and Bauer P 2014 The effect of converter efficiency on DEAP-based energy conversion: an overview and optimization method **9056** 90561D
[17] Todorcevic T, van Kessel R, Bauer P and Ferreira J A 2015 A modulation strategy for wide voltage output in DAB-based dc-dc modular multilevel converter for DEAP wave energy conversion *Emerg. Sel. Top. Power Electron. IEEE J.* **3** 1171–81
[18] Madsen F B, Daugaard A E, Hvilsted Słoren and Skov A L 2016 The current state of silicone-based dielectric elastomer transducers *Macromol. Rapid Commun.* **37** 378–413
[19] Rosset S and Shea H R 2013 Flexible and stretchable electrodes for dielectric elastomer actuators *Appl. Phys.* A **110** 281–307
[20] Brown R W 2007 Distributed circuit modeling of multilayer capacitor parameters related to the metal film layer *IEEE Trans. Compon. Packag. Technol.* **30** 764–73
[21] Carpi F *et al* 2015 Standards for dielectric elastomer transducers *Smart Mater. Struct.* **24** 105025

[22] Schlaak H F, Gei M, Bortot E, Haus H and Mößinger H 2016 *Dielectric Elastomers as EAPS: Models* Book Section 32 Polymers and Polymeric Composites: A Reference Series (Cham: Springer Nature) p 715
[23] Haus H, Matysek M, Mößinger H and Schlaak H F 2013 Modelling and characterization of dielectric elastomer stack actuators *Smart Mater. Struct.* **22** 104009
[24] Graf C and Maas J 2012 A model of the electrodynamic field distribution for optimized electrode design for dielectric electroactive polymer transducers *Smart Mater. Struct.* **21** 094001
[25] Sullivan C R, Sun Y and Kern A M 2002 Improved distributed model for capacitors in high-performance packages *Conf. Record of the 2002 Industry Conf. 37th IAS Annual Meeting* vol **2** pp 969–76 (https://doi.org/10.1109/IAS.2002.1042675)
[26] Menardo P, Fourmon A, Jean P, and Wattez A Rigid to elastic electrode connection, 02/08/2012 WO/2012/101474